Original Article

Improvement of Whole-body Bone Planar Images on a Bone-dedicated Single-photon Emission Computed Tomography Scanner by Blind Deconvolution Algorithm

Zhexin Wang[1,2], Hui Liu[1,2], Li Cheng[3], Zhenlei Lyu[1], Lilei Gao[3], Nianming Jiang[1,3], Zuoxiang He[2,4], Yaqiang Liu[1,2]

[1]Department of Engineering Physics, Tsinghua University, [2]Institute for Precision Medicine, Tsinghua University, [3]Beijing Novel Medical Equipment Ltd., Beijing, China, [4]School of Clinical Medicine, Tsinghua University, Beijing, China

Abstract

Purpose: We have developed a bone-dedicated collimator with higher sensitivity but slightly degraded resolution on single-photon emission computed tomography (SPECT) for planar bone scintigraphy, compared with conventional low-energy high-resolution collimator. In this work, we investigated the feasibility of using the blind deconvolution algorithm to improve the resolution of planar images on bone scintigraphy. **Materials and Methods:** Monte Carlo simulation was performed with the NCAT phantom for modeling bone scintigraphy on the clinical dual-head SPECT scanner (Imagine NET 632, Beijing Novel Medical Equipment Ltd.) equipped with the bone-dedicated collimator. Maximum likelihood estimation method was used for the blind deconvolution algorithm. The initial estimation of point spread function (PSF) and iteration number for the method were determined by comparing the deblurred images obtained from different input parameters. We simulated different tumors in five different locations and with five different diameters to evaluate the robustness of the initial inputs. Furthermore, we performed chest phantom studies on the clinical SPECT scanner. The quantified increased contrast ratio (CR) between the tumor and the background was evaluated. **Results:** The 2 mm PSF kernel and 10 iterations provided a practical and robust deblurred image on our system. Those two inputs can generate robust deblurred images in terms of the tumor location and size with an average increased CR of 21.6%. The phantom studies also demonstrated the ability of blind deconvolution, using those two inputs, with increased CRs of 17%, 17%, 22%, 20%, and 13% for lesions with diameters of 1 cm, 2 cm, 3 cm, 4 cm, and 5 cm, respectively. **Conclusions:** It is feasible to use the blind deconvolution algorithm to deblur the planar images for SPECT bone scintigraphy. The appropriate values of the PSF kernel and the iteration number for the blind deconvolution can be determined using simulation studies.

Keywords: Blind deconvolution, planar images, single-photon emission computed tomography, whole-body bone scintigraphy

Received on: 24-09-2023 **Review completed on: 15-01-2024** **Accepted on: 14-02-2024** **Published on: 30-03-2024**

Introduction

Single-photon emission computed tomography (SPECT) bone scanning, which is widely used in metabolic bone disease, traumatology, bone and joint infections, and particularly in oncology, is one of the most common examinations in nuclear medicine imaging.[1] As shown in Figure 1, there are two main categories of bone scans, namely, planar bone scintigraphy and three-dimensional tomography;[2] planar bone scintigraphy is used routinely in clinic due to its simplicity.[3]

Clinical whole-body bone scintigraphy is a multi-bed imaging technology that captures multiple projections of the entire skeleton. However, this technology usually requires a long scanning time to obtain a reasonable planar image due to the poor sensitivity of SPECT scanner. Moreover, it reduces the examination efficiency and patient comfort, increases the possibility of patient motion during the examination, and causes motion artifact.[4] Efforts to improve the sensitivity of SPECT scanners have focused on collimator design, which is the critical factor, with proposals for dedicated collimators of high sensitivity in bone scintigraphy. However, commercially

Access this article online

Quick Response Code:

Website: www.jmp.org.in

DOI: 10.4103/jmp.jmp_127_23

Address for correspondence: Dr. Hui Liu, Department of Engineering Physics, Tsinghua University, Beijing 100084, China. Institute for Precision Medicine, Tsinghua University, Beijing 100084, China. E-mail: liuhui2020@tsinghua.edu.cn

How to cite this article: Wang Z, Liu H, Cheng L, Lyu Z, Gao L, Jiang N, *et al*. Improvement of whole-body bone planar images on a bone-dedicated single-photon emission computed tomography scanner by blind deconvolution algorithm. J Med Phys 2024;49:110-9.

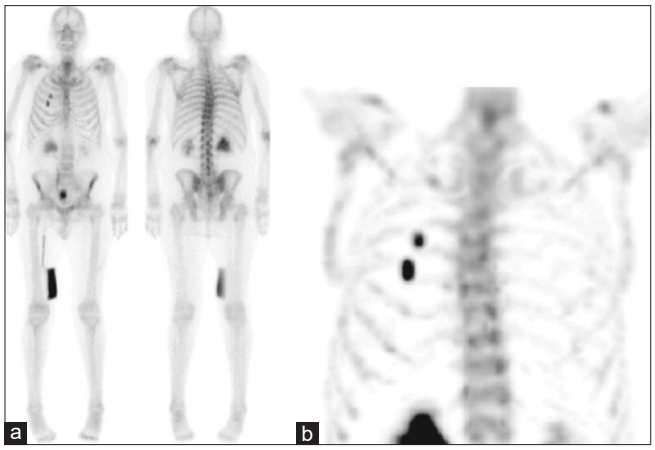

Figure 1: (a) Anterior and posterior two-dimensional planar images of whole-body bone scintigraphy, (b) maximum intensity projection image of the three-dimensional tomographic image from single-photon emission computed tomography bone scanning

available collimators may show a slight degradation in resolution limited by the tradeoff between collimator sensitivity and resolution.[5]

Recently, we have developed a dedicated, parallel-hole collimator for bone scintigraphy on a clinical dual-head SPECT system (Imagine NET 632, Beijing Novel Medical Equipment Ltd.), which has a sensitivity of 177 cpm/μCi, better than the conventional, low-energy, high-resolution collimator. However, the resolution is higher than 9.5 mm, which will have an impact on image sharpness and clinical diagnosis. The research on improving resolution has always been a research hotspot such as the use of pinhole collimators,[6] four-head SPECT,[7] and self-collimating SPECT.[8] Nevertheless, some of these methods lose detection sensitivity while achieving high resolution, and others are only at a theoretical or research stage and too far from clinical application. Moreover, our research is conducted under the condition that the system design has already been determined, so we will not consider redesigning the system. Other algorithms, such as reconstruction with hybrid kernelized expectation maximization or deep learning,[9,10] can improve the resolution from 10 to 5 mm even to positron emission tomography level but have limited effects on planar images.

Considering the blurring effect of low resolution, it is potentially feasible to apply the blind deconvolution approach to the planar images to improve the resolution of bone scintigraphy. While blind deconvolution has been extensively applied in various fields of image and signal processing, including radio astronomy, seismology, and biomedical engineering, it is rarely used in the nuclear imaging field.[11] Furthermore, for SPECT planar images, the practical point spread function (PSF) is unknown and difficult to estimate due to the distance-dependent response.

The blind deconvolution algorithm is a multi-solution problem, which means multiple combinations of PSF and recovered images can generate the same convolution output. An appropriate deconvolution greatly depends on the initial estimation of the PSF and the number of iterations, whereas the iteration number is also related to the noise in the recovered images due to the high noise in SPECT images. Many efforts have been made to improve the practicality of the algorithm.[12] Several new iterative formulas have been proposed to improve the basic implementation of the algorithm[13-16] based on simulation studies. To enhance the convergence speed and stability, vector extrapolation principles,[17] prior information from deep learning,[18-21] and constraints from the L0-norm and total variation[22-27] are also utilized to enhance convergence speed and stability. In addition, a two-step blind deconvolution[28-31] has been proposed recently, resulting in faster algorithms with improved robustness.

While these prior studies have indicated promising results, they have not delved into the issue of selecting key parameters, such as the initial PSF estimation and iteration number, especially for deblurring SPECT planar images with high noise. In this work, we investigated the feasibility of the blind deconvolution approach for deblurring SPECT planar images to enhance the quality of bone scintigraphy using the bone-dedicated collimator we have developed. We aimed to produce a simple, convenient, and clinically applicable approach based on blind deconvolution that can significantly improve the planar image quality of our SPECT system. Compared with other algorithms, our proposed deconvolution approach is much easier for the implementation and more stable for the output.

Materials and Methods

Single-photon emission computed tomography scanner

The clinical dual-head SPECT scanner (Imagine NET 632) with bone-dedicated collimators was used in this study. The system consists of two detectors, composed of NaI (Tl) crystals with a size of 585 mm × 470 mm × 9.5 mm. The effective field of view (FOV) area is 520 mm × 400 mm. The distance between the center of FOV and the surface of collimator is 20 mm. The energy resolution is 9.8% at 140 keV. The intrinsic spatial resolution is 3.4 mm at central FOV. The dedicated collimator for bone scanning is a type of parallel-hole collimator, with a thickness of 25.5 mm, hole size of 1.22 mm, and hole thickness of 0.16 mm.

Blind deconvolution

We proposed the blind deconvolution algorithm is to obtain a deblurred image based on maximum likelihood estimation.[32] The iterative formulae are as follows:[33,34]

$$i^{(k+1)}(x,y)=\left[\frac{p(x,y)}{i^{(k)}(x,y)*h^{(k)}(x,y)}*h^{(k)}(x,y)\right]\times i^{(k)}(x,y) \quad (1)$$

$$h^{(k+1)}(x,y)=\left[\frac{p(x,y)}{i^{(k)}(x,y)*h^{(k)}(x,y)}*i^{(k)}(x,y)\right]\times h^{(k)}(x,y) \quad (2)$$

where k is the number of iterations, $i^{(k)}(x,y)$ is the deblurred

image obtained after the k^{th} iteration, $h^{(k)}(x, y)$ is the PSF acquired after the k^{th} iteration, and $p(x, y)$ is the initial planar image, which is to be deblurred.

In practical application, its discrete form is used:

$$i^{(k+1)}(x, y) = \left[\sum_{t=0}^{T-1} \sum_{q=0}^{Q-1} \frac{p(t,q)}{\sum_{m=0}^{M-1} \sum_{n=0}^{N-1} i^{(k)}(m, n)\, g^{(k)}(t - m, q - n)} \times h^{(k)}(x - t, y - q) \right] \times i^{(k)}(x, y) \quad (3)$$

$$h^{(k+1)}(x, y) = \left[\sum_{t=0}^{T-1} \sum_{q=0}^{Q-1} \frac{p(t,q)}{\sum_{m=0}^{M-1} \sum_{n=0}^{N-1} i^{(k)}(m, n)\, h^{(k)}(t - m, q - n)} \times i^{(k)}(x - t, y - q) \right] \times h^{(k)}(x, y) \quad (4)$$

$(x = 0, 1, 2\ldots\ldots T-1; y = 0, 1, 2\ldots\ldots Q-1)$

where k is the number of iterations, $i^{(k)}(x, y)$ is the deblurred image obtained after the k^{th} iteration, and $h^{(k)}(x, y)$ is the PSF acquired after the k^{th} iteration. $P(t, q)$ is the initial planar image, which is to be deblurred. T, Q, M, and N are the total number of pixels in each dimension.

While the initial estimation of the deblurred image, PSF, and the iteration number is critical for the blind deconvolution algorithm, we established those values to be close to the targeted values according to the physical process of SPECT scanning.

The original image acquired by SPECT is directly applied as the initial estimation of the deblurred image. The two-dimensional PSF was modeled as a zero mean Gaussian function, determined by the convolution kernel σ and the truncated dimension. Although the practical resolution for the projection is difficult to estimate because the SPECT collimator resolution is distance dependent, the resolution range can be calculated with the resolution formula. Then, the range of the convolution kernel, where the initial PSF convolution kernel σ should be located, can be obtained. In our study, first, considering the collimating effect of the collimator, it is assumed that the collimator only receives γ photon from the vertical direction, and then, the phantom thickness is known. Hence, the range of the convolution kernel can be calculated by the resolution formula. The convolution kernel σ should be located at $1.41 \text{ mm} \leq \sigma \leq 2.92 \text{ mm}$. The truncated dimension is greater than three σ. Meanwhile, we used a limited iteration number to avoid amplification noise, whereas our initial inputs are close to the target based on the above design.

GEANT4 Application for Tomographic Emission simulation

To evaluate the performance of the proposed blind deconvolution approach, we performed Monte Carlo simulation studies with the GEANT4 Application for Tomographic Emission platform (8.1 version).[35] The SPECT scanner (Imagine NET 632 scanner) with bone-dedicated collimators for data acquisition was simulated. The energy resolution is 9.8% at 140 keV. The two detectors were placed opposite to each other. As shown in Figure 2, the NCAT phantom with ^{99m}technetium methylene diphosphonate tracer was used for bone scintigraphy, whereas several different tumors were inserted into the skeleton. The ratio of activity between tumor, bone, and background was set to be 450:90:2. The size of the phantom was 51.2 cm × 51.2 cm × 40 cm. The attenuation and scatter of the phantom were modeled. The data acquisition energy window was 126–154 keV. Herein, we focus on the projection of a single-bed position for our algorithm evaluation.

Experiments and evaluation

Comparison of different input parameters

To examine the effect of different inputs on the deconvoluted output and to test the validity of the proposed prediction scheme, we implemented the blind deconvolution approach using various input parameters, which are the initial PSF and iteration number, on a single original projection. The planar image obtained from the simulation with NCAT phantom is shown in Figure 3. The image voxel size is 4.0625 mm × 4.0625 mm. The total activity (emission count) in our simulation was 66,000 Bq, and the scanning time was 150 s.

Evaluation with different tumors

To further validate the robustness of the proposed approach, we implemented the blind deconvolution in multiple scenarios by varying the tumor location and size in simulations. We inserted the tumors with a diameter of 4 cm into different

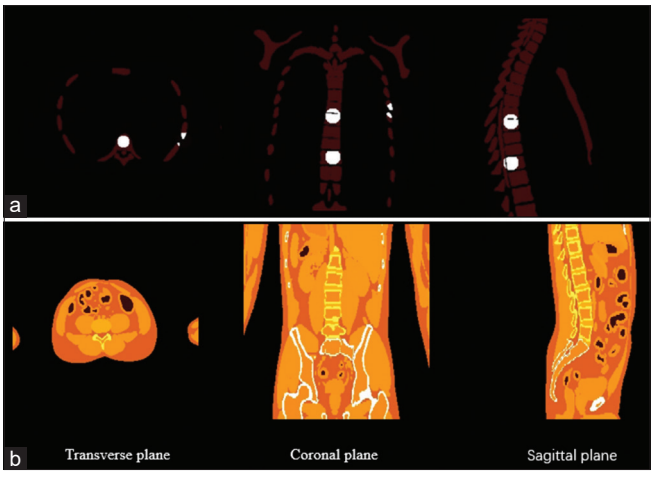

Figure 2: (a) The activity image of the NCAT phantom, (b) the attenuation coefficient image of the NCAT phantom. The white regions in activity image indicate tumors with a diameter of approximately 4 cm

body regions, including the lower leg, thigh, pelvis, vertebral bones, and neck to verify the impact of tumor location. Then, we changed the diameter of the tumor in the vertebral bones from 1 to 5 cm with a 1-cm interval to verify the impact of the tumor size.

Chest phantom experiments

We designed and manufactured a custom chest phantom, as shown in Figure 4. The regions of the ribs and vertebral bones inside the phantom were injected with the ^{99m}technetium solution with a total activity of 10.12 mCi. The activity ratio between the tumor and background was 3:1. The phantom was positioned at the FOV center of the clinical dual-head SPECT system described above (Imagine NET 632), equipped with our designed bone-dedicated collimators. The acquisition time was set to 30 s.

Quantification evaluation

We quantified the increased contrast ratio (ΔCR) of the tumor after the implementation of the blind deconvolution algorithm, as Equation (5), with the CR defined as the mean activity A_t of the tumor region over the mean activity A_b of the background region based on the projection image.

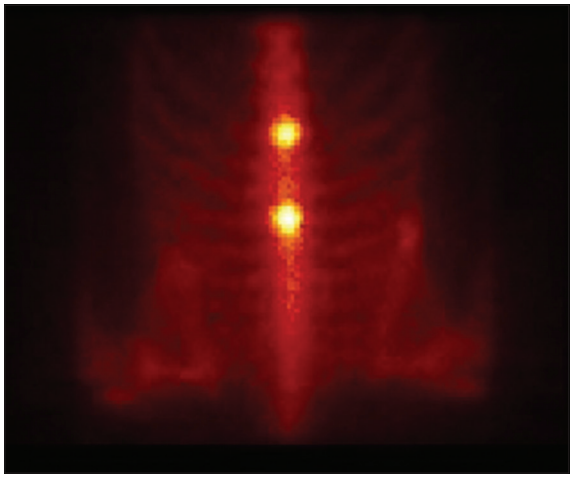

Figure 3: A typical planar image of the NCAT phantom obtained on our bone-dedicated single-photon emission computed tomography scanner

$$\Delta CR = \frac{CR_{debluured} - CR_{initial}}{CR_{initial}} \quad (5)$$

where $CR_{debluured}$ is the CR of the tumor after blind deconvolution and $CR_{initial}$ is the CR before blind deconvolution. The size of the background region was the same as that of the tumor region. The ideal CR is 3 (same as the activity ratio between the tumor and background set above).

The surrounding area of the tumor region with low uptake is chosen as background.

Results

Comparison of different input parameters

As shown in Figure 5, all obtained projection images demonstrated improved image quality and quantified increased CR after blind deconvolution with various initial PSF inputs and iteration numbers. However, different inputs had a significant impact on the image quality. The blind deconvolution algorithm with small iteration numbers or small kernel PSF cannot fully deblur the image, whereas the algorithm with large iteration numbers increased the noise. Furthermore, image distortion was observed with the large kernel PSF. Visually, the blind deconvolution algorithm with 2 mm PSF and 10 iterations provided the best tradeoff between image resolution and image noise. Therefore, we determined the initial PSF input as the PSF with 2 mm kernel and an iteration number of 10 for our bone-dedicated collimator. In Figure 6, we present the two profiles across the spinal region with tumor and the rib region. The differences between the tumor regions and the spine and the rib regions were greater, and the image details were clearer. The improvement in the peak and the valley was significant after blind deconvolution.

Evaluation of different tumor locations

In Figure 7, all the projection images for each tumor obtained at the five different positions demonstrated an improved tumor detection ability after blind deconvolution. In addition, due to the differences in inter-phantom attenuation for the tumor at different sites, the improvements differed slightly, particularly for the tumor in the neck. Quantified

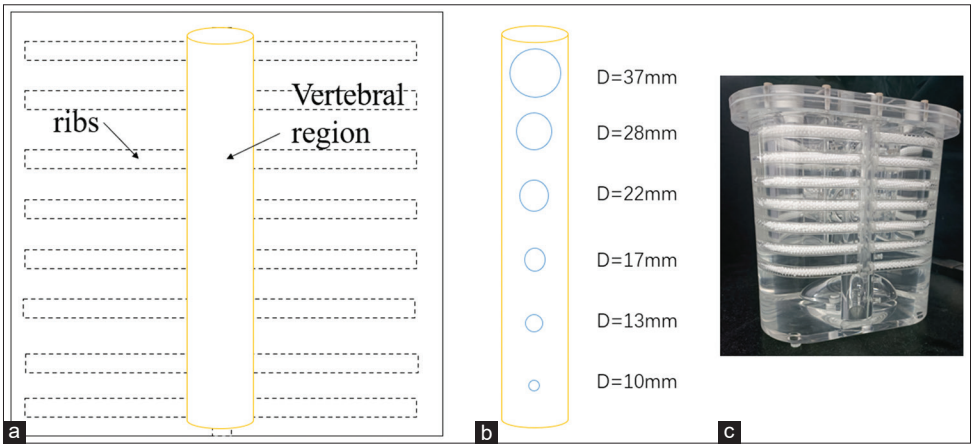

Figure 4: (a) Front view of the vertebral region, (b) vertebral components, blue circles representing the spherical lesions, (c) the photo of phantom

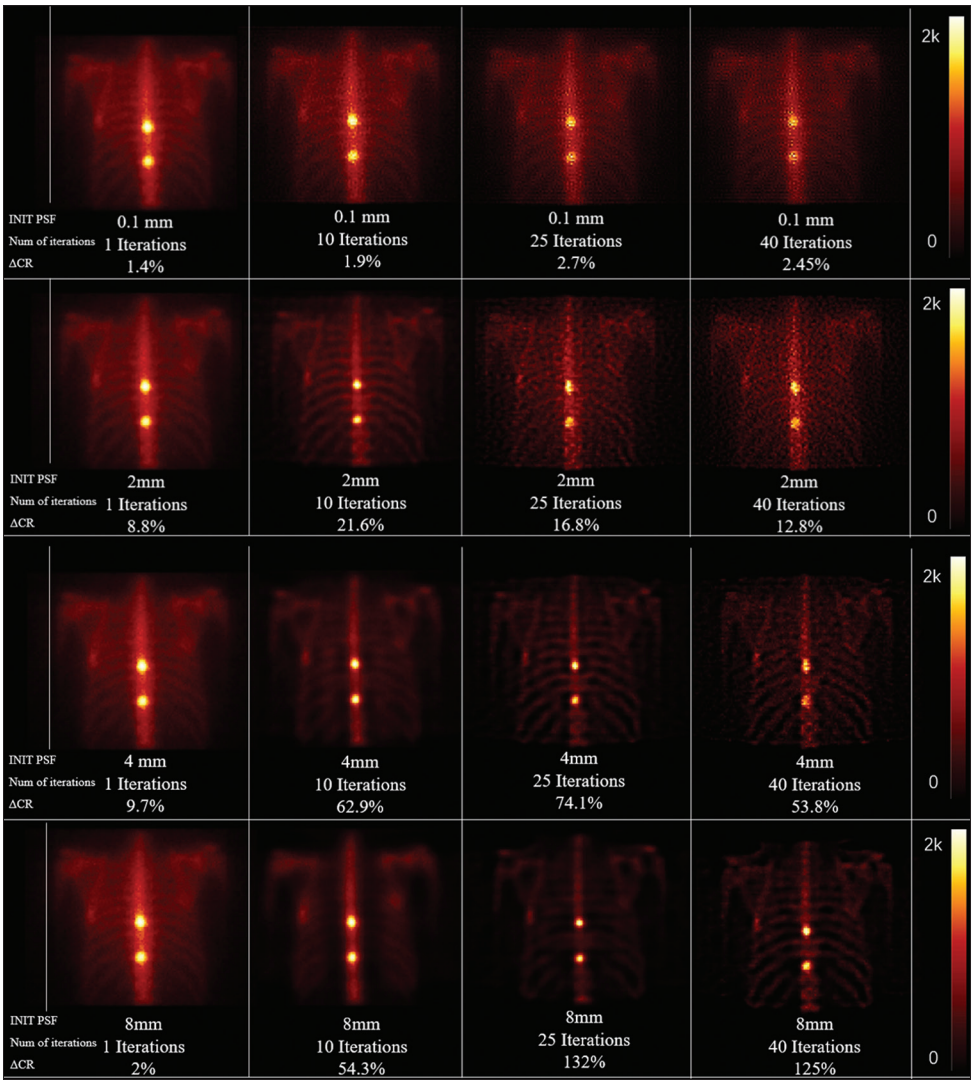

Figure 5: The results of different input parameters. The parameters are given under each deblurred images: The quantified increased contrast ratio(ΔCR), iteration numbers, the INIT PSF which means the initial convolution kernel used for the deconvolution. The unit of color bar is counts, presenting the number of events detected. PSF: Point spread function, CR: Contrast ratio

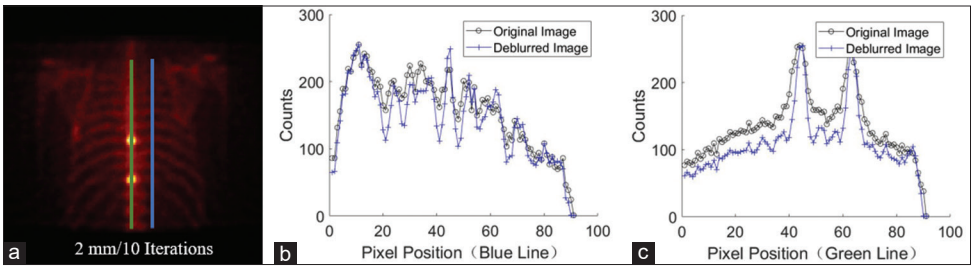

Figure 6: Deblurred images (a) and two profiles (b and c) of the original image and the deblurred images obtained from blind deconvolution

increased CRs also demonstrated the same trend, as shown in Figure 8. The blind deconvolution algorithm was effective in improving the CRs in tumor and nontumor regions at different sites.

Evaluation of different tumor sizes

Figure 9 shows the output images after the blind deconvolution algorithm for tumors of five different diameters. The image counts fluctuated more obviously after implementation of the blind deconvolution. The results demonstrated that the initial PSF kernel was feasible for blind deconvolution of the projection images of our bone-dedicated collimator in terms of different tumor sizes. The increased activity ratios after blind deconvolution were also stable, as shown in Figure 10.

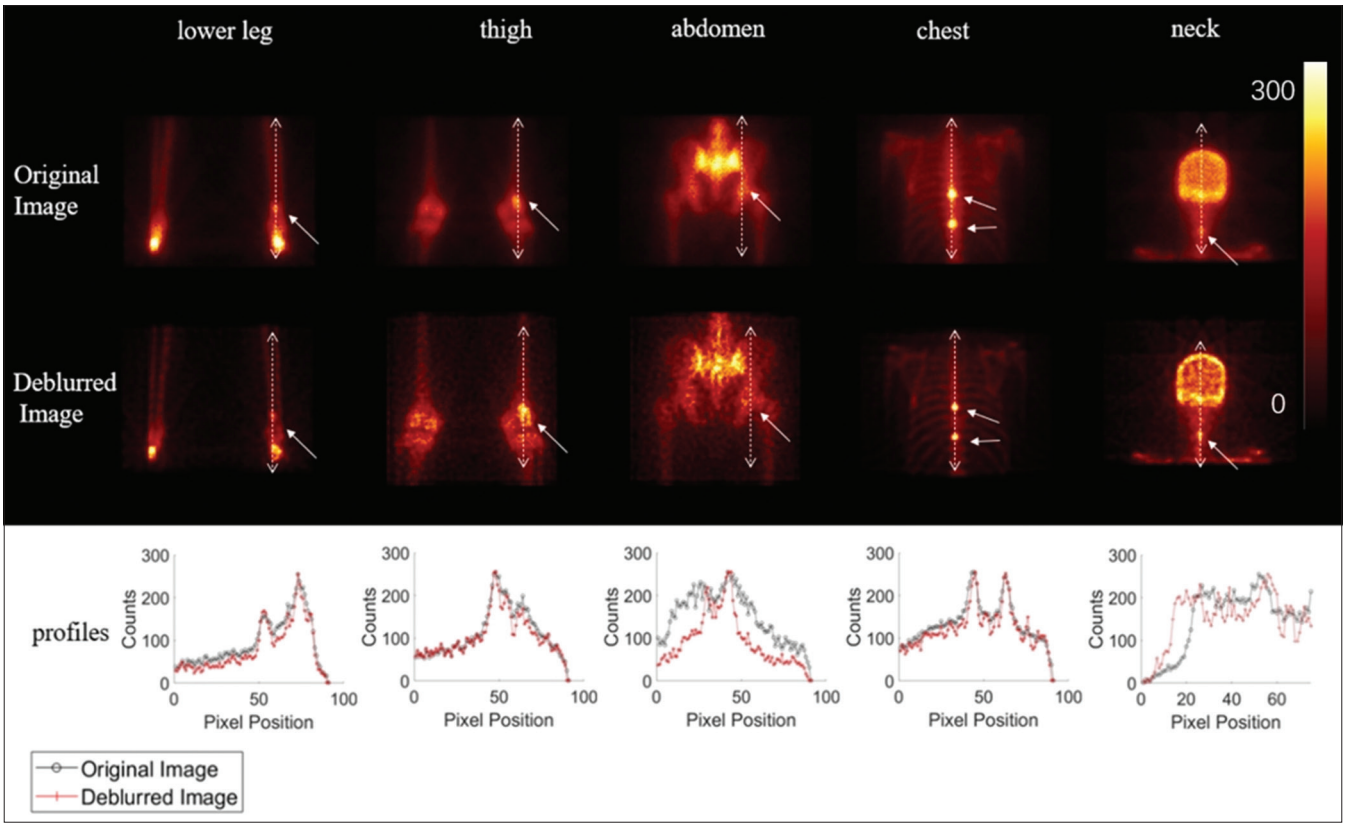

Figure 7: Comparison before and after blind deconvolution for different tumor positions. The unit of color bar is counts, presenting the number of events detected. The five columns share the same color bar. In the upper part of the image, the bidirectional arrow represents the section line, while the unidirectional arrow points to the location of the tumor. The lower part of the image shows the counts corresponding to the position of the section line

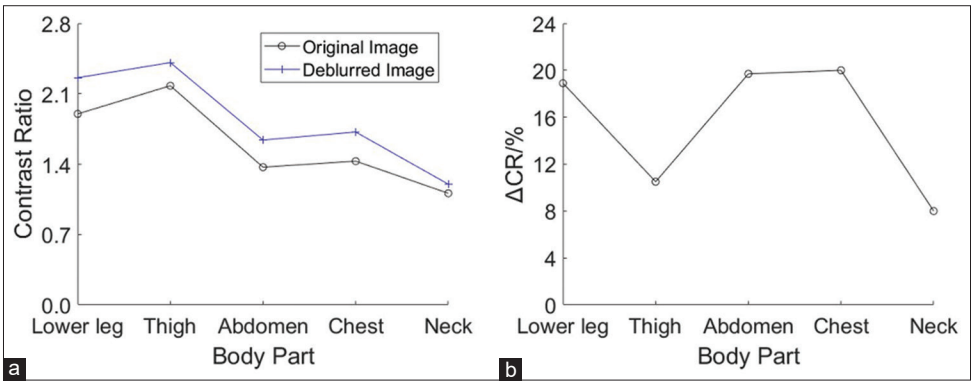

Figure 8: (a) Contrast ratios before and after deconvolution at different sites, (b) increased contrast ratios before and after the algorithm at different sites

Phantom experiments

The six hot spherical lesions outlined by the blue squares were numbered 1–6, from top to bottom in Figure 11. The six hot spherical lesions have a horizontal offset in the radial of the vertebral components. Because they require one end to be connected to the vertebral components, drugs are injected through the small holes in the connecting part. The CRs and ΔCR were calculated, as shown in Figure 12. The ribs in the background region appeared clearer. The blind deconvolution algorithm showed improvements in CRs for the six hot spherical lesions of varying sizes, consistent with the results of the Monte Carlo simulations.

Discussion

In this study, we aimed to adopt the blind deconvolution algorithm to improve the quality of planar imaging for SPECT bone scanning using the bone-dedicated collimator we designed. Based on the simulation studies, we found that the 2 mm PSF kernel and 10 iterations provided a reasonable and robust deblurred image with our system, whereas the initial inputs are critical factors for the performance of the blind deconvolution algorithm. Furthermore, the determined inputs were verified with the phantom studies on the clinical SPECT scanner with the bone-dedicated collimator. The results demonstrated the ability of the blind deconvolution

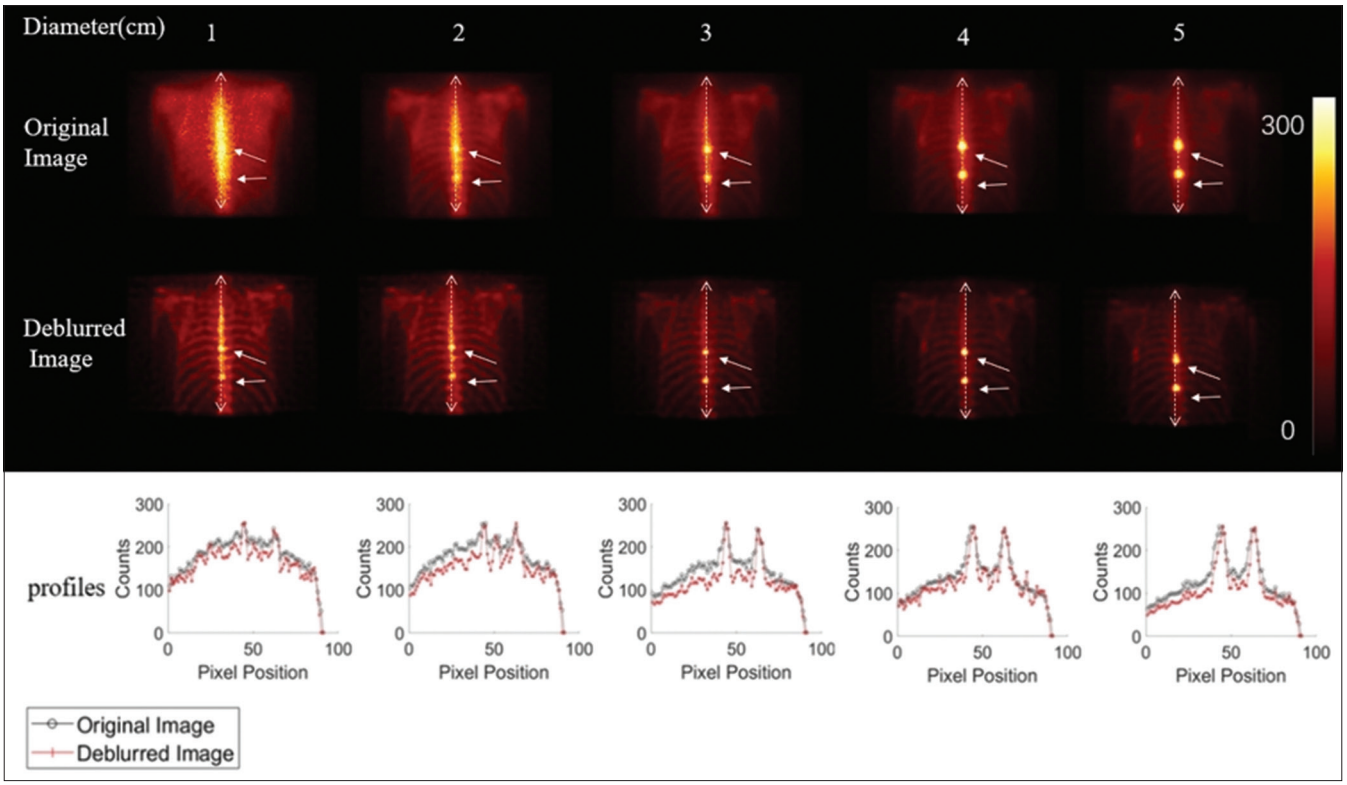

Figure 9: Comparison before and after blind deconvolution for different tumor sizes. The unit of color bar is counts, presenting the number of events detected. The five columns share the same color bar. In the upper part of the image, the bidirectional arrow represents the section line, while the unidirectional arrow points to the location of the tumor. The lower part of the image shows the counts corresponding to the position of the section line

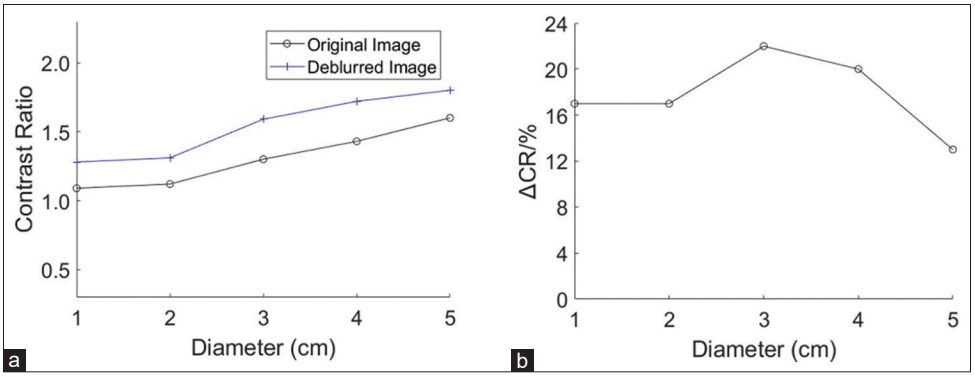

Figure 10: (a) Contrast ratios before and after deconvolution for different tumor diameters, (b) increased contrast ratios before and after the algorithm for different tumor diameters

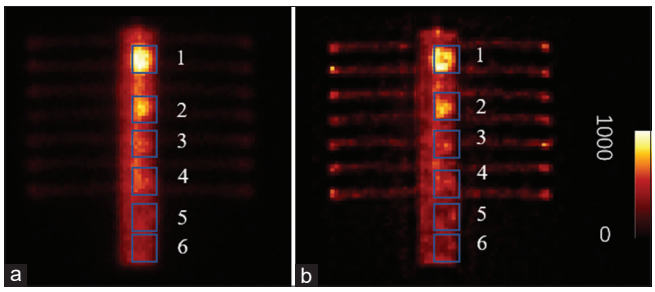

Figure 11: (a) Original image obtained in clinic, (b) output image after blind deconvolution. Six bone (hot) lesions outlined by blue squares were used to calculate contrast ratios. Numbers 1–6 are the lesion numbers in this phantom. The unit of color bar is counts presenting the number of events detected. The a and b share the same color bar

algorithm to deblur the planar images of SPECT bone scintigraphy.

However, those input parameters might not be feasible for other SPECT system planar imaging, or even the same SPECT system equipped with other collimators. To examine that, we simulated planar images of the NCAT phantom on the SPECT scanner but using five different collimators, as shown in Table 1. The NCAT phantom with a 3-cm-diameter tumor in the vertebral bones was used. As shown in Figures 13 and 14, there were apparent differences across those systems, although all the deblurred images showed an improvement. The number 1 system with low resolution had low original activities but showed a marked increase. In contrast, the number 3 system with high resolution exhibited high initial

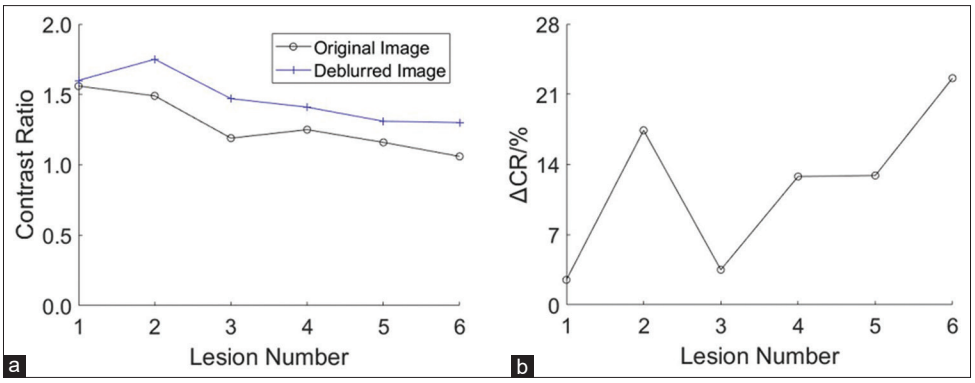

Figure 12: (a) Contrast ratios before and after deconvolution, (b) increased activity ratios before and after the algorithm

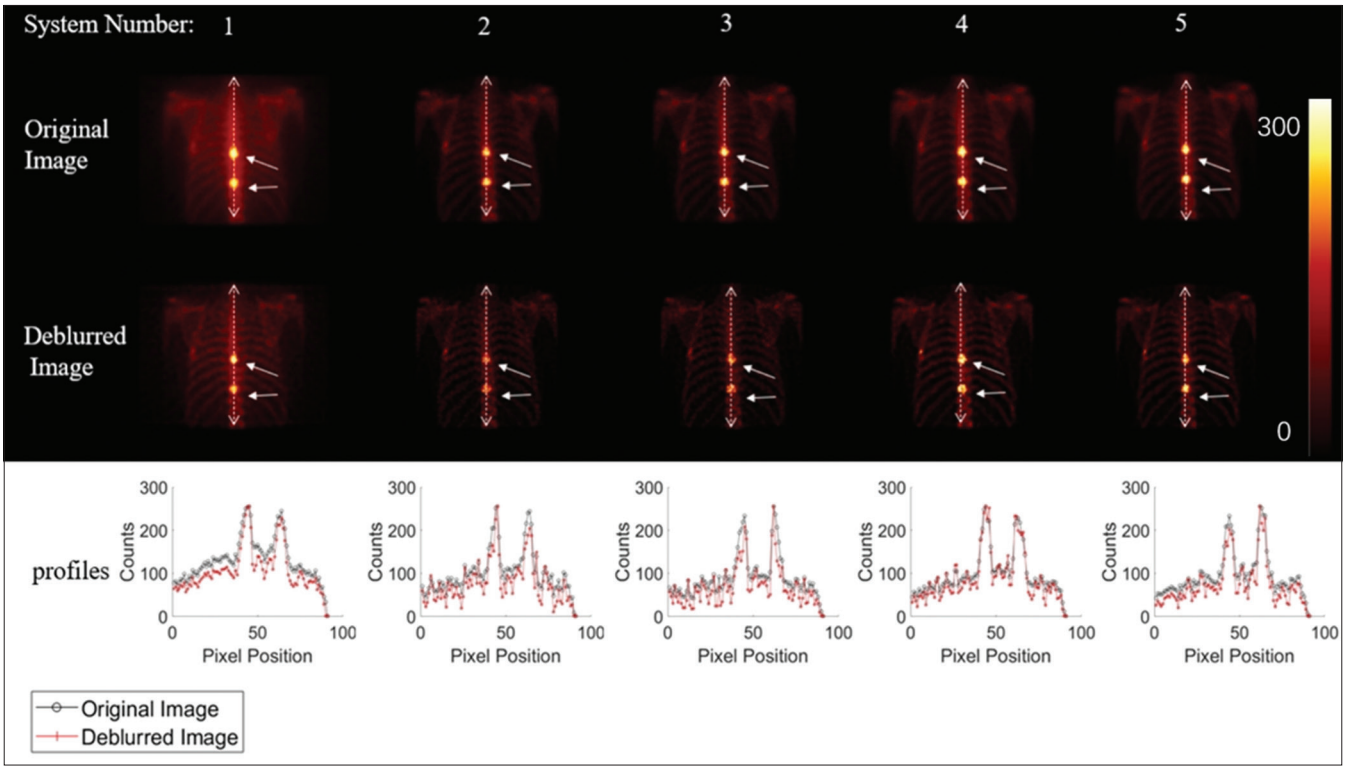

Figure 13: Comparison before and after blind deconvolution for different single-photon emission computed tomography collimators. The unit of color bar is counts, presenting the number of events detected. The five columns share the same color bar. In the upper part of the image, the bidirectional arrow represents the section line, while the unidirectional arrow points to the location of the tumor. The lower part of the image shows the counts corresponding to the position of the section line

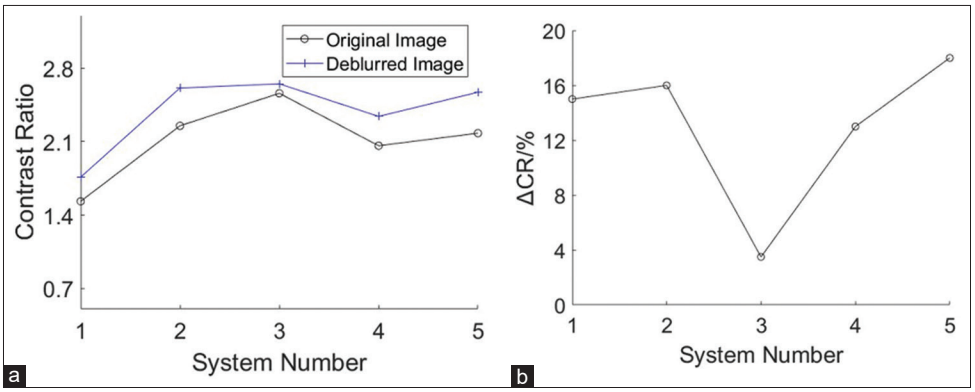

Figure 14: (a) Contrast ratios before and after deconvolution for different systems, (b) increased contrast ratios before and after algorithm for different single-photon emission computed tomography collimators

Table 1: Collimator parameters

System number	Thickness (mm)	Hole thickness (mm)	Hole size (mm)	Kernel minimum	Kernel maximum
1	35.0	0.20	0.75	1.57	3.04
2	27.0	0.15	0.50	1.50	2.68
3	28.5	0.15	0.50	1.50	2.60
4	25.5	0.20	0.50	1.50	2.76
5	25.5	0.25	0.50	1.50	2.76

activity, but the increase after the blind deconvolution was limited.

From the results presented above, we can conclude that the blind deconvolution algorithm is a suitable method to deblur the planar images of SPECT bone scintigraphy for its consistency of imaging principles of the SPECT and the improvement of the blurred images. However, its improvement effect is limited, and there is no significant improvement effect on images obtained with high-resolution systems. However, some other algorithms such as reconstruction with hybrid kernelized expectation maximization or deep learning methods can also be used to improve the resolution. Our proposed deconvolution approach is much easier for the implementation and the output results would be more stable.

Conclusions

In this investigation, we aimed to adopt the blind deconvolution algorithm to improve the quality of planar imaging for SPECT bone scanning. We determined the most appropriate values of the PSF kernel and iteration number as inputs for blind deconvolution using our bone-dedicated collimator based on simulation studies. The results of the phantom studies demonstrated the ability of the blind deconvolution algorithm to deblur the planar images of SPECT bone scintigraphy.

Acknowledgments

This work was supported in part by the National Key Research and Development Program of China (No. 2022YFC2402002), the National Natural Science Foundation of China (No. 12205166), and the Tsinghua Precision Medicine Foundation (2022PY002).

Financial support and sponsorship

Nil.

Conflicts of interest

There are no conflicts of interest.

References

1. Wang J, Li S. A brief report on the results of the national survey of nuclear medicine in 2020. Chin J Nucl Med Mol Imaging 2020;40:747-9.
2. Rager O, Nkoulou R, Exquis N, Garibotto V, Tabouret Viaud C, Zaidi H, *et al.* Whole-body SPECT/CT versus planar bone scan with targeted SPECT/CT for metastatic workup. BioMed Research International, vol. 2017, Article ID 7039406, 8 pages, 2017.
3. O'Connor MK, Brown ML, Hung JC, Hayostek RJ. The art of bone scintigraphy – Technical aspects. J Nucl Med 1991;32:2332-41.
4. Wang Z,Liu H, Cheng L, Gao L, Lyu Z, Jiang N. Design of dedicated collimator for whole-body bone scanning on single photonemission computed tomography based on monte carlo simulation. J Tsinghua Univ (Sci Technol) 2023;63:811-7.
5. Cherry SR, Sorenson JA, Phelps ME, & ScienceDirect (Online service). Physics in nuclear medicine (Vol. 3). Saunders; 2003.
6. Chen Y, Goorden MC, Vastenhouw B, Beekman FJ. Optimized sampling for high resolution multi-pinhole brain SPECT with stationary detectors. Phys Med Biol 2020;65:015002.
7. Massari R, D'Elia A, Soluri A, & Soluri A. Super Spatial Resolution (SSR) method for small animal SPECT imaging: A Monte Carlo study. Nuclear Instruments and Methods in Physics Research Section A: Accelerators, Spectrometers, Detectors and Associated Equipment 2020;982:164584.
8. Ma T, Wei Q, Lyu Z, Zhang D, Zhang H, Wang R, *et al*. Self-collimating SPECT with multi-layer interspaced mosaic detectors. IEEE Transactions on Medical Imaging 2021;40:2152-69.
9. Marquis H, Deidda D, Gillman A, Willowson KP, Gholami Y, Hioki T, *et al.* Theranostic SPECT reconstruction for improved resolution: Application to radionuclide therapy dosimetry. EJNMMI Phys 2021;8:16.
10. Shao W, Du Y. SPECT image reconstruction by deep learning using a two-step training method. J Nuclear Med 2019;60 Suppl 1:1353.
11. Jansson PA. Deconvolution of Images and Spectra. New York: Courier Corporation; 2014.
12. Barmby P, McLaughlin DE, Harris WE, Harris GL, & Forbes DA. Structural parameters for globular clusters in M31 and generalizations for the fundamental plane. The Astronomical Journal 2007;133:2764.
13. Holmes TJ. Blind deconvolution of quantum-limited incoherent imagery: Maximum-likelihood approach. J Opt Soc Am A 1992;9:1052-61.
14. Dempster AP, Laird NM, Rubin DB. Maximum likelihood from incomplete data via the EM algorithm. J R Stat Soc Ser B (Methodol) 1977;39:1-22.
15. Mignotte M, Meunier J. A Comparison of Supervised and Blind Deconvolution Techniques Applied in SPECT Imagery. Département D'informatique et de Reserche Opérationnelle (DIOR), Université de Montréal. Montréal, PQ, Canada: Technologies Report; 1999.
16. Bronstein MM, Bronstein AM, Zibulevsky M, Zeevi YY. Blind deconvolution of images using optimal sparse representations. IEEE Trans Image Process 2005;14:726-36.
17. Biggs DS, Andrews M. Acceleration of iterative image restoration algorithms. Appl Opt 1997;36:1766-75.
18. Sun L, Cho S, Wang J, & Hays J. (2013). Edge-based blur kernel estimation using patch priors. In IEEE international conference on computational photography (ICCP) (pp. 1-8). IEEE
19. Pan J, Sun D, Pfister H, & Yang MH. (2016). Blind image deblurring using dark channel prior. In Proceedings of the IEEE conference on computer vision and pattern recognition (pp. 1628-1636).
20. Ren D, Zhang K, Wang Q, Hu Q, & Zuo W. (2020). Neural blind deconvolution using deep priors. In Proceedings of the IEEE/CVF Conference on Computer Vision and Pattern Recognition (pp. 3341-3350).
21. Zuo, W., Ren, D., Gu, S., Lin, L., & Zhang, L. (2015). Discriminative learning of iteration-wise priors for blind deconvolution. In Proceedings of the IEEE conference on computer vision and pattern recognition (pp. 3232-3240).
22. Dong W, Tao S, Xu G, Chen Y. Blind deconvolution for poissonian blurred image with total variation and L(0)-Norm gradient regularizations. IEEE Trans Image Process 2021;30:1030-43.

23. Jin M, Roth S, Favaro P. Normalized Blind Deconvolution. In Proceedings of the European Conference on Computer Vision (ECCV); 2018.
24. Pan J, Hu Z, Su Z, & Yang MH. (2014). Deblurring text images via L0-regularized intensity and gradient prior. In Proceedings of the IEEE Conference on Computer Vision and Pattern Recognition (pp. 2901-2908).
25. Perrone D, Favaro P. Total Variation Blind Deconvolution: The Devil is in the Details. In Proceedings of the IEEE Conference on Computer Vision and Pattern Recognition; 2014.
26. Chowdhury MR, Qin J, Lou Y. Non-blind and blind deconvolution under poisson noise using fractional-order total variation. J Math Imaging Vis 2020;62:1238-55.
27. Xu L, Zheng S, Jia J. Unnatural l0 Sparse Representation for Natural Image Deblurring. In Proceedings of the IEEE Conference on Computer Vision and Pattern Recognition; 2013.
28. Krishnan D, Tay T, Fergus R. Blind Deconvolution Using a Normalized Sparsity Measure. In CVPR 2011. IEEE; 2011.
29. Chan TF, Wong CK. Total variation blind deconvolution. IEEE Trans Image Process 1998;7:370-5.
30. Fergus R, Singh B, Hertzmann A, Roweis ST, & Freeman WT. (2006). Removing camera shake from a single photograph. In Acm Siggraph 2006 Papers (pp. 787-794).
31. Levin A, Weiss Y, Durand F, & Freeman WT. Efficient marginal likelihood optimization in blind deconvolution. In CVPR 2011 (pp. 2657-2664). IEEE. (2011).
32. Van Trees HL. Detection, Estimation, and Modulation Theory, Part I: Detection, Estimation, and Linear Modulation Theory. USA: John Wiley & Sons; 2004.
33. Holmes TJ, Bhattacharyya S, Cooper JA, Hanzel D, Krishnamurthi V, Lin WC, & Turner JN. (1995). Light microscopic images reconstructed by maximum likelihood deconvolution. In: Handbook of biological confocal microscopy,Springer, Boston, MA 1995. p: 389-402.
34. Shepp LA, Vardi Y. Maximum likelihood reconstruction for emission tomography. IEEE Trans Med Imaging 1982;1:113-22.
35. Jan S, Santin G, Strul D, Staelens S, Assié K, Autret D, *et al.* GATE: A simulation toolkit for PET and SPECT. Phys Med Biol 2004;49:4543-61.